

Towards Clinical Practice in CT-Based Pulmonary Disease Screening: An Efficient and Reliable Framework

Qian Shao^{*,1}, Bang Du^{*,1}, Yixuan Wu¹, Zepeng Li¹, Qiyuan Chen¹, Qianqian Tang²,
Jian Wu^{†,1}, Jintai Chen³, Hongxia Xu^{†,1},

¹Zhejiang University ²Shaoxing Tangtang Technology Co., Ltd. ³The Hong Kong University of Science and Technology
Email: {qianshao, wujian2000, einstein}@zju.edu.cn

Abstract—Deep learning models for pulmonary disease screening from Computed Tomography (CT) scans promise to alleviate the immense workload on radiologists. Still, their high computational cost, stemming from processing entire 3D volumes, remains a major barrier to widespread clinical adoption. Current sub-sampling techniques often compromise diagnostic integrity by introducing artifacts or discarding critical information. To overcome these limitations, we propose an Efficient and Reliable Framework (ERF) that fundamentally improves the practicality of automated CT analysis. Our framework introduces two core innovations: (1) A Cluster-based Sub-Sampling (CSS) method that efficiently selects a compact yet comprehensive subset of CT slices by optimizing for both representativeness and diversity. By integrating an efficient k -nearest neighbor search with an iterative refinement process, CSS bypasses the computational bottlenecks of previous methods while preserving vital diagnostic features. (2) An Ambiguity-aware Uncertainty Quantification (AUQ) mechanism, which enhances reliability by specifically targeting data ambiguity arising from subtle lesions and artifacts. Unlike standard uncertainty measures, AUQ leverages the predictive discrepancy between auxiliary classifiers to construct a specialized ambiguity score. By maximizing this discrepancy during training, the system effectively flags ambiguous samples where the model lacks confidence due to visual noise or intricate pathologies. Validated on two public datasets with 2,654 CT volumes across diagnostic tasks for 3 pulmonary diseases, ERF achieves diagnostic performance comparable to the full-volume analysis (over 90% accuracy and recall) while reducing processing time by more than 60%. This work represents a significant step towards deploying fast, accurate, and trustworthy AI-powered screening tools in time-sensitive clinical settings.

Index Terms—Pulmonary disease screening, sub-sampling, uncertainty quantification

I. INTRODUCTION

Deep learning has shown great promise in automating pulmonary disease screening from CT scans, potentially alleviating the immense workload on radiologists [1], [2]. However, the standard practice of processing entire 3D volumes is computationally prohibitive, hindering deployment in time-sensitive or resource-constrained clinical settings [3], [4]. Unlike radiologists, who quickly skim to focus on relevant slices, full-volume approaches waste resources on diagnostically irrelevant data. Therefore, developing intelligent methods

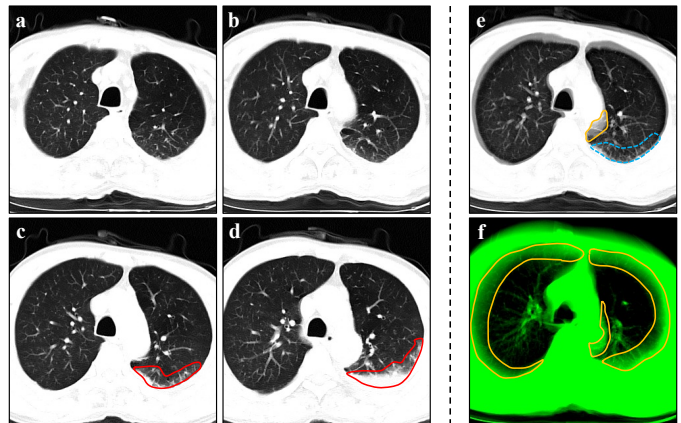


Fig. 1. Visualization of interpolation methods on common pneumonia (CP) lesions. (a-d) are four consecutive slices showing CP lesions (red solid-line area). (e) and (f) are results of spline interpolation and projection interpolation, respectively. Yellow solid lines indicate processing-induced artifacts, blue dashed lines highlight regions of lesion elimination post-processing.

to select salient diagnostic information is crucial for practical clinical integration.

Prior work on sub-sampling often compromises diagnostic integrity. Interpolation techniques can introduce artifacts or erase critical details [5], as shown in Fig. 1, while conventional slice selection relies on rigid heuristics [6], [7]. Although recent machine learning utilizes representativeness or diversity [8], [9], they face three key limitations: (1) Focusing exclusively on representativeness causes redundancy, while solely prioritizing diversity risks missing collective diagnostic signals [10]. (2) Calculating pairwise similarities for selection contradicts the goal of efficiency [11], [12]. (3) Neglecting lung anatomy leads to incoherent sub-sampling, degrading downstream performance [7].

The challenge of using reduced data subsets elevates the need for robust uncertainty quantification (UQ). However, existing UQ methods like Bayesian Neural Networks [13] or Deep Ensembles (DE) [14] are computationally too expensive for efficient screening pipelines [15]. More importantly, standard metrics like predictive entropy often fail to specifically capture data ambiguity arising from subtle lesions or artifacts, which are common in medical imaging. Without explicitly

*Equal contributions. †Corresponding author.

flagging these ambiguous cases, a model operating on partial data risks making overconfident yet incorrect predictions.

To address these challenges, we propose an Efficient and Reliable Framework (ERF). First, to ensure **diagnostic integrity efficiently**, we design a Cluster-based Sub-Sampling (CSS) method. CSS first partitions the lung volume based on anatomical structure. Within each part, CSS employs K -Means to group slices [12] and an efficient approximate k -NN search algorithm based on Hierarchical Navigable Small World (HNSW) graphs [16] to identify the most representative slice in each cluster. An iterative refinement process then optimizes for diversity, ensuring the subset is both compact and comprehensive without heavy computation. Second, to guarantee **reliability**, we introduce an Ambiguity-aware Uncertainty Quantification (AUQ) mechanism. Inspired by discrepancy-maximization in domain adaptation [17], [18], we employ two auxiliary classifiers alongside the primary model. By training these auxiliary heads to maximize their predictive discrepancy, we force them to expose decision boundaries sensitive to ambiguity. This discrepancy serves as a precise proxy for data ambiguity, which we combine with the primary classifier’s predictive entropy to form a robust, low-overhead uncertainty score.

We validate ERF on two public datasets totaling 2,654 CT volumes for three pulmonary diseases. Experiments demonstrate that ERF achieves diagnostic performance (over 90% accuracy and recall) comparable to full-volume analysis while reducing processing time by over 60%. Furthermore, the visualization results demonstrate that CSS can select representative CT slices containing crucial indicators to aid in diagnosis. The main contributions are:

- We develop ERF, a framework balancing high efficiency with diagnostic accuracy for pulmonary screening.
- We propose CSS to hierarchically select representative and diverse CT slices, bypassing computational bottlenecks of prior methods.
- We design AUQ, which leverages classifier discrepancy to specifically quantify data ambiguity and model uncertainty with minimal overhead.
- Extensive validation confirms ERF matches full-volume performance with significantly reduced computational cost.

II. RELATED WORKS

A. Pulmonary Disease Screening

Deep learning has established 3D CT as the preferred modality for pulmonary screening due to its rich anatomical detail [2], [19]. State-of-the-art models have achieved remarkable success in detecting diverse pathologies, ranging from interstitial and obstructive diseases [20], [21] to neoplastic and infectious conditions [22], [23]. However, the substantial computational overhead of processing high-resolution volumetric data remains a critical bottleneck.

B. Sub-Sampling

To alleviate the computational burden, data reduction techniques are widely adopted. Classical approaches rely on

interpolation [5], [24], [25] or heuristic slice selection [6], [7]. While interpolation acts as a generalized sub-sampling method, it risks introducing artifacts, whereas heuristic selection often disrupts volumetric continuity, potentially omitting small but critical lesions.

Learning-based sampling offers a more sophisticated alternative, generally categorized by objectives of representativeness or diversity. Representative sampling minimizes statistical discrepancies between the subset and the full volume, *e.g.*, Wasserstein [26] or energy [27] distance, maximum mean discrepancy [28], and generalized empirical F -discrepancy [10]. Conversely, diversity sampling seeks to maximize information content by selecting varied samples [9]. Despite these advancements, generic sampling algorithms typically disregard task-specific anatomical priors. They treat CT scans as unstructured data distributions, failing to preserve the structural context essential for accurate medical diagnosis.

C. Uncertainty Quantification

UQ [29], [30] is vital for deploying deep learning models in critical applications like medical diagnosis, enabling them to signal low confidence. Prominent UQ approaches include Bayesian Neural Networks [13], [31], Monte Carlo (MC) Dropout [32], and DE [14]. While powerful, these methods introduce significant computational overhead, such as requiring multiple forward passes for inference or training multiple models, which dramatically increases resource consumption [33]. Other notable methods include evidential deep learning [34], which aims for single-pass uncertainty, and conformal prediction [35], providing model-agnostic guarantees but whose utility depends on calibration.

III. METHODS

Our proposed ERF operates in two stages: CSS first compresses volumetric data into informative slices via iterative density-diversity optimization. Subsequently, AUQ employs a discrepancy-maximization mechanism to perform robust classification while explicitly flagging data ambiguity.

A. Cluster-based Sub-Sampling

Given a dataset of N CT volumes $\mathcal{D} = \{(\mathbf{x}_i, \mathbf{y}_i)\}_{i=1}^N$, where each volume \mathbf{x}_i contains n slices, our goal is to select a subset of $m \ll n$ representative and diverse slices to approximate the full-volume diagnostic performance. CSS achieves this through a structured, iterative process involving anatomical partitioning, clustering, and refined selection.

1) *Partitioning and Representation*: To preserve anatomical semantics, we first partition each volume into upper, middle, and lower regions based on a fixed ratio (0.25 : 0.15 : 0.6), distributing the selection budget m proportionally. Subsequently, we map each slice \mathbf{s}_j to a feature vector $\mathbf{h}_j \in \mathbb{R}^d$ using the image encoder of a frozen, pre-trained MedCLIP-ViT [36], normalized such that $\|\mathbf{h}_j\|_2 = 1$. This inference-only step ensures high-level semantic capture with minimal computational overhead.

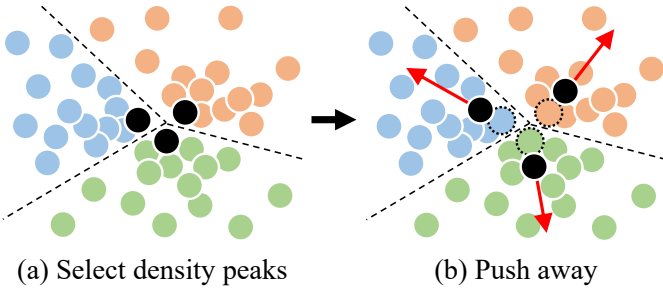


Fig. 2. The core insight of CSS. Density peaks are selected for representativeness, and then they are pushed away via an iterative refinement process for diversity. The dashed and solid black circles denote the selected instances from the previous iteration and the current iteration, respectively.

2) *Iterative Selection via Density and Diversity*: CSS operates on the principle that selected slices should be both representative (density peaks) and diverse (covering the feature space). First, we partition the slice features within each anatomical region into clusters using K -Means. Let C_k denote the k -th cluster. We aim to select one instance $z \in C_k$ that best balances local density and global diversity.

a) *Representativeness*: We estimate the local density of an instance z using the Euclidean distance to its k -NN, denoted as $D(z, z|k)$. Minimizing this distance identifies density peaks. To ensure scalability, we employ Hierarchical Navigable Small World (HNSW) graphs [16] for approximate k -NN search.

b) *Diversity Refinement*: Selecting only density peaks may yield redundant slices if clusters are semantically close. We introduce an iterative refinement process. Let $Z^{(t)}$ be the set of selected instances at iteration t . For a candidate instance z in cluster C_k , we define a diversity regularizer $\Phi(z, t)$ that penalizes proximity to instances selected from *other* clusters in the previous iteration:

$$\Phi(z, t) = \sum_{\tilde{z} \in Z^{(t-1)} \setminus C_k} \frac{1}{\|z - \tilde{z}\|_2^\alpha}, \quad (1)$$

where $Z^{(t-1)} \setminus C_k$ denotes the set of previously selected instances excluding the one belonging to cluster C_k , and α is a sensitivity hyperparameter controlling the strength of the distance penalty. This term is stabilized via an Exponential Moving Average (EMA) [37] with momentum β :

$$\bar{\Phi}(z, t) = \beta \cdot \bar{\Phi}(z, t-1) + (1 - \beta) \cdot \Phi(z, t). \quad (2)$$

c) *Selection Objective*: At each iteration t , we update the selection for cluster C_k by maximizing a joint objective:

$$\tilde{z}^{(k,t)} = \arg \max_{z \in \mathcal{N}_h(\tilde{z}^{(k,t-1)})} \left[\frac{1}{D(z, z|k)} - \lambda \cdot \bar{\Phi}(z, t) \right], \quad (3)$$

where λ balances representativeness and diversity. To further accelerate computation, the search space is restricted to the h nearest neighbors \mathcal{N}_h of the currently selected instance. The final subset $\tilde{\mathcal{D}}$ is formed after T iterations.

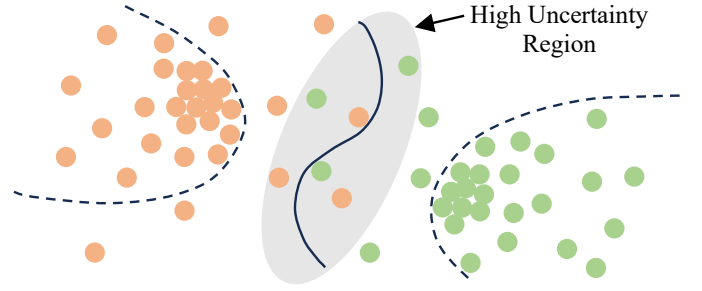


Fig. 3. Illustration of AUQ. The circles of different colors represent samples from distinct categories. The solid and dashed lines denote the decision hyperplanes generated by the main and auxiliary classifiers, respectively. High-uncertainty samples are located in the gray area.

B. Ambiguity-aware Uncertainty Quantification (AUQ)

While the selected subset $\tilde{\mathcal{D}}$ enables efficient screening, subsampling inherently introduces ambiguity. Standard entropy metrics often fail to capture ambiguity, *e.g.*, artifacts, subtle lesions. We propose AUQ to explicitly quantify this ambiguity via classifier discrepancy.

a) *Framework*: We augment the primary classifier G with two auxiliary classifiers G_1 with parameter matrix \mathbf{W}_1 and G_2 with \mathbf{W}_2 . All classifiers share the feature extractor F but possess distinct prediction heads. The primary model is trained via standard cross-entropy \mathcal{L}_{CE} . The model architecture is shown in the Technical Appendix.

b) *Discrepancy Maximization*: To capture ambiguity, we force G_1 and G_2 to diverge on ambiguous samples while maintaining accuracy. We define the discrepancy d_{dis} as the mean L_1 -distance between the probability vectors $\mathbf{p}^1, \mathbf{p}^2$ and the primary prediction \mathbf{p} , following [38]:

$$d_{dis}(\mathbf{p}_i^1, \mathbf{p}_i^2) = \frac{1}{N_{\text{cls}}} (\|\mathbf{p}_i^1 - \mathbf{p}_i\|_1 + \|\mathbf{p}_i^2 - \mathbf{p}_i\|_1 + \|\mathbf{p}_i^1 - \mathbf{p}_i^2\|_1), \quad (4)$$

where N_{cls} is the number of classes. To operationalize this, we formulate the training objective for the auxiliary classifiers:

$$\min_{\mathbf{W}_1, \mathbf{W}_2} \frac{1}{N} \sum_{i=1}^N (\mathcal{L}_{CE}(\mathbf{p}_i^1, \mathbf{y}_i) + \mathcal{L}_{CE}(\mathbf{p}_i^2, \mathbf{y}_i) - d_{dis}(\mathbf{p}_i^1, \mathbf{p}_i^2)). \quad (5)$$

Crucially, gradients from the discrepancy term are detached from the backbone F to prevent degrading the shared representation.

c) *Uncertainty Score*: High discrepancy indicates that the input $\tilde{\mathbf{x}} \in \tilde{\mathcal{D}}$ lies near decision boundaries sensitive to subtle variations. We combine this ambiguity proxy with predictive entropy \mathcal{H} for a robust uncertainty score $U(\tilde{\mathbf{x}})$:

$$U(\tilde{\mathbf{x}}) = d_{dis}(\mathbf{p}^1, \mathbf{p}^2) + \mathcal{H}(\tilde{\mathbf{x}}). \quad (6)$$

This score allows ERF to flag uncertain cases, providing a more reliable basis for clinical decision-making.

IV. EXPERIMENTS

A. Datasets and Tasks.

We validate our framework on two public datasets: SARS-CoV-2 [39] and LUNG-PET-CT-Dx [40]. Excluding volumes

TABLE I

COMPARISON WITH OTHER SUB-SAMPLING METHODS. THE BEST PERFORMANCE IS BOLD, AND THE SECOND-BEST PERFORMANCE IS UNDERLINED, EXCEPT FOR THE FULL CT METHOD. EACH RESULT SHOWS MEAN ACCURACY AND STANDARD DEVIATION OVER 5-FOLD CROSS-VALIDATION.

Method	Task 1		Task 2		Task 3	
	Accuracy	Recall	Accuracy	Recall	Accuracy	Recall
Full CT	99.12 \pm 0.31	99.15 \pm 0.35	99.35 \pm 0.41	99.30 \pm 0.38	92.47 \pm 0.60	92.10 \pm 0.65
PI	90.36 \pm 0.34	89.02 \pm 0.41	88.92 \pm 0.40	89.00 \pm 0.30	84.59 \pm 0.47	83.50 \pm 0.52
LI	78.52 \pm 2.54	77.89 \pm 2.67	73.67 \pm 2.03	71.70 \pm 2.30	68.81 \pm 3.80	67.54 \pm 4.81
SI	98.78 \pm 0.34	98.20 \pm 0.37	98.33 \pm 0.42	98.30 \pm 0.40	87.24 \pm 0.40	86.94 \pm 0.37
SSS	96.89 \pm 0.56	96.28 \pm 0.62	95.23 \pm 0.97	95.12 \pm 0.99	89.34 \pm 0.90	89.67 \pm 1.24
ESS	96.42 \pm 0.86	96.85 \pm 0.78	94.29 \pm 1.37	94.50 \pm 1.70	88.56 \pm 1.56	86.78 \pm 1.65
CoreSet	97.38 \pm 0.47	96.39 \pm 0.59	98.06 \pm 0.47	97.57 \pm 0.77	88.91 \pm 1.88	89.07 \pm 2.06
ActiveFT	98.75 \pm 0.38	98.26 \pm 0.76	98.62 \pm 0.36	98.38 \pm 0.61	90.68 \pm 0.71	90.35 \pm 1.14
CSS (Ours)	98.89\pm0.17	99.05\pm0.18	98.65\pm0.23	98.82\pm0.29	91.88\pm0.43	90.85\pm0.54

TABLE II

COMPARISON WITH OPTIMAL METHODS OF OTHER TYPES UNDER A LOWER SUB-SAMPLING RATE.

Task	Method	Accuracy	Recall
Task 1	SI	97.99 \pm 0.85	98.06 \pm 0.54
	SSS	95.38 \pm 0.46	94.78 \pm 0.56
	ActiveFT	98.00 \pm 0.48	97.32 \pm 0.47
	CSS (Ours)	98.13\pm0.66	98.13\pm0.30
Task 2	SI	96.73 \pm 0.95	97.10 \pm 0.79
	SSS	94.11 \pm 0.90	94.06 \pm 0.89
	ActiveFT	97.18 \pm 0.22	97.17 \pm 0.56
	CSS (Ours)	97.68\pm0.36	98.11\pm0.88
Task 3	SI	83.63 \pm 1.24	83.49 \pm 1.33
	SSS	76.36 \pm 1.68	77.16 \pm 1.86
	ActiveFT	84.73 \pm 1.15	85.21 \pm 1.29
	CSS (Ours)	90.03\pm0.40	90.35\pm1.14

with insufficient depth (< 64 slices), we curate a dataset of 2,654 CT scans, comprising 747 Novel Coronavirus Pneumonia (NCP), 741 Common Pneumonia (CP), 311 Adenocarcinoma (AC), and 855 normal cases. We formulate three binary classification tasks to evaluate diagnostic versatility: Task 1 (NCP vs. Normal), Task 2 (CP vs. Normal), and Task 3 (AC vs. Normal). For each task, we employ 5-fold cross-validation, reporting mean accuracy and recall. Implementation details are provided in the Technical Appendix.

B. Comparison with Other Sub-Sampling Methods

We compare CSS against different sub-sampling baselines. The baselines include three widely-used interpolation methods: Projection Interpolation (PI) [5], Linear Interpolation (LI) [24], and Spline Interpolation (SI) [25], two heuristic slice selection methods: Subset Slice Selection (SSS) [6] and Even Slice Selection (ESS) [7], two representative and diverse sub-sampling methods: CoreSet [8] and ActiveFT [11]. We also include the full CT method as an upper-bound reference. For a fair comparison, all sub-sampling methods select 64 slices per volume, except for the full CT method, since it utilizes the complete CT data. The same classification backbone and training hyperparameters are used for all experiments.

As shown in Table I, CSS consistently outperforms other sub-sampling methods, approaching the performance of using

TABLE III

COMPARISON WITH OTHER UQ METHODS.

Method	Task 1	Task 2	Task 3
Entropy	50.79 \pm 9.44	67.74 \pm 10.78	57.95 \pm 4.72
Discrepancy	<u>74.76\pm15.91</u>	77.18 \pm 10.25	<u>77.69\pm7.72</u>
DE	73.73 \pm 16.41	69.60 \pm 8.11	67.56 \pm 8.89
MC Dropout	70.95 \pm 4.18	<u>78.65\pm5.88</u>	66.28 \pm 8.07
AUQ (Ours)	94.92\pm7.05	91.59\pm7.93	92.05\pm5.45

the full CT volume. A notable performance drop is observed for all methods in Task 3 (adenocarcinoma detection) compared to Tasks 1 and 2 (pneumonia diagnosis). We attribute this to the inherent difficulty of Task 3, which involves identifying smaller, morphologically complex lesions, a challenge corroborated by our qualitative results in Fig. 4.

We further challenge our method by reducing the sampling budget to 32 slices. As shown in Table II, while other methods degrade rapidly, CSS exhibits strong robustness. In Task 3, CSS achieves a significant margin over the second-best ActiveFT (+5.30% accuracy, +5.14% recall). This suggests that our strategy effectively identifies the most informative slices even when the budget is extremely tight. Additional experiments with 16, 8, 4 slices are provided in the Appendix.

C. Comparison with Other UQ Methods

We compare AUQ with Entropy, Discrepancy-only, Deep Ensemble (DE) [14], and MC Dropout [32]. To quantify the effectiveness of UQ in flagging errors, we introduce misdiagnosis recall $\text{Recall}_{\text{mis}}$. Specifically, we select the top-15 most uncertain samples and calculate the recall of actual misclassified cases ($FN + FP$) within this subset. A higher $\text{Recall}_{\text{mis}}$ indicates the method correctly assigns high uncertainty to erroneous predictions. To ensure fairness, we fix the backbone predictions across all UQ methods. Table III demonstrates that AUQ significantly outperforms baselines, including computationally expensive DE, confirming that AUQ effectively captures data ambiguity.

D. Efficiency Evaluation

We analyze the computational complexity and actual inference time to demonstrate the efficiency of ERF.

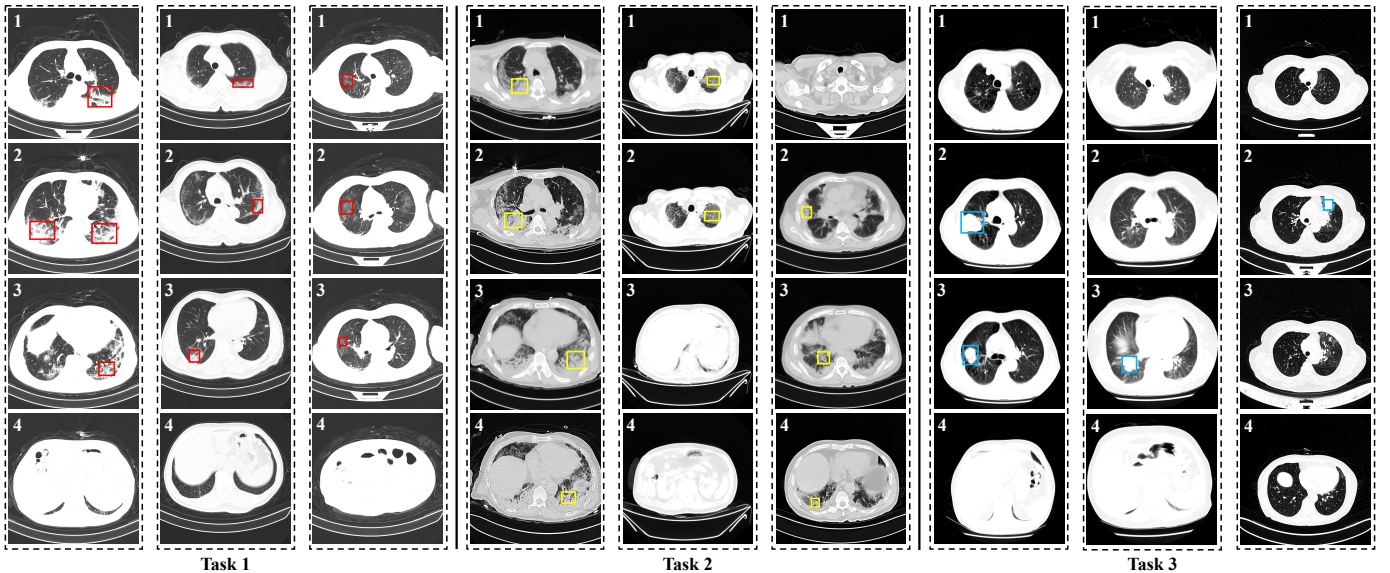


Fig. 4. CT slices selected by CSS. The red, yellow, and blue boxes mark the lesion areas of NCP, CP, and AC, respectively.

TABLE IV
TIME COMPLEXITY COMPARISON.

Sub-Sampling	Complexity	UQ Method	Complexity
Full CT	$O(N \cdot n)$	Entropy	$O(N \cdot n)$
SI	$O(N \cdot n)$	Discrepancy	$O(N \cdot n)$
SSS	$O(N \cdot m)$	DE	$O(N \cdot n \cdot M_{DE})$
ActiveFT	$O(N \cdot n^2)$	MC Dropout	$O(N \cdot n \cdot M_{MC})$
CSS (Ours)	$O(N \cdot n \log n)$	AUQ (Ours)	$O(N \cdot n)$

TABLE V
INFERENCE TIME FOR 50 CASES.

Method	Task 1	Task 2	Task 3
SI	52.83s (31%)	55.35s (29%)	53.68s (30%)
SSS	41.52s (25%)	42.78s (23%)	41.76s (23%)
ActiveFT	81.28s (48%)	87.57s (46%)	82.37s (46%)
CSS (Ours)	66.64s (39%)	70.88s (37%)	67.53s (38%)
Full CT	169.24s	189.05s	179.25s

1) *Complexity Analysis*: Table IV presents the asymptotic time complexity, where M_{DE} represents the number of models that DE ensembles, and M_{MC} represents the number of MC Dropout forward passes. For sub-sampling, CSS ($O(N \cdot n \log n)$) is significantly more efficient than ActiveFT ($O(N \cdot n^2)$), as our HNSW-based search avoids exhaustive pairwise comparisons. For UQ, AUQ maintains the efficiency of single-pass methods, avoiding the linear cost scaling of DE (M_{DE}) and MC Dropout (M_{MC}).

2) *Runtime Comparison*: In addition, we calculate the inference times of CSS, and the optimal methods of other types (*i.e.*, SI, SSS, and ActiveFT). The inference time of ActiveFT and CSS comprises three components: (1) Feature extraction time using the pre-trained MedCLIP-ViT; (2) Time taken to select 32 slices based on their respective strategies; (3) Time for disease detection by the classification model. The inference time of the SI and SSS methods only includes the time for

slice selection (or interpolation) and model classification. The full CT method’s computation time only includes the inference time of the classification model. Table V reports the inference time for processing 50 cases, where the percentage represents the proportion of the full CT method’s time. While Full CT yields high accuracy, its reliance on 3D convolutions results in prohibitive latency ($> 169s$). CSS reduces this time by over 60%. Although slightly slower than simple heuristic methods (SI, SSS), CSS provides a far better trade-off, ensuring high diagnostic accuracy with acceptable latency, as shown in Table I. Compared to ActiveFT, CSS is faster due to the efficient approximate nearest neighbor search.

E. Visualization

We visualize the CT slices selected by CSS in Fig. 4, where each case retains 4 slices. The selected slices accurately capture the lesion areas (marked in colored boxes) for all three diseases. Consistent with quantitative results, NCP and CP present larger, more obvious lesions, whereas AC manifests as smaller, localized nodules. The ability of CSS to pinpoint these subtle AC lesions confirms its effectiveness.

V. CONCLUSIONS

In this work, we introduce ERF, a framework designed to confront the dual impediments of computational expense and model trust that currently hinder the widespread clinical adoption of deep learning for pulmonary disease screening. Our approach makes two primary contributions. First, we propose CSS, which curates a compact yet diagnostically potent subset of CT slices by optimizing for both representativeness and diversity. Second, we design a lightweight AUQ mechanism for our task, which captures data ambiguity arising from subtle lesions or artifacts. Our extensive validation on two public datasets demonstrates that ERF not only matches the diagnostic performance of full-volume analysis but also reduces

inference time by over 60%. More critically, ERF's ability to reliably identify and flag uncertain predictions represents a pivotal step toward the deployment of fast, accurate, and trustworthy AI in real-world clinical workflows.

REFERENCES

- [1] Huaying Hao, Yitian Zhao, Shaoyi Leng, Yuanyuan Gu, Yuhui Ma, Feiming Wang, Qi Dai, Jianjun Zheng, Yue Liu, and Jingfeng Zhang, "Local salient location-aware anomaly mask synthesis for pulmonary disease anomaly detection and lesion localization in ct images," *Medical Image Analysis*, vol. 102, pp. 103523, 2025.
- [2] Medhat A Tawfeek, Ibrahim Alrashdi, Madallah Alruwaili, Warda M Shaban, and Fatma M Talaat, "Enhancing the efficiency of lung cancer screening: predictive models utilizing deep learning from ct scans," *Neural Computing and Applications*, pp. 1–19, 2025.
- [3] K Balasamy and V Seethalakshmi, "Hco-rlf: Hybrid classification optimization using recurrent learning and fuzzy for covid-19 detection on ct images," *Biomedical Signal Processing and Control*, vol. 100, pp. 106951, 2025.
- [4] Nhat Truong Pham, Jinsol Ko, Masaud Shah, Rajan Rakkiyappan, Hyun Goo Woo, and Balachandran Manavalan, "Leveraging deep transfer learning and explainable ai for accurate covid-19 diagnosis: Insights from a multi-national chest ct scan study," *Computers in Biology and Medicine*, vol. 185, pp. 109461, 2025.
- [5] Vitali Liauchuk, "Imageclef 2019: Projection-based ct image analysis for tb severity scoring and ct report generation.," in *CLEF (Working Notes)*, 2019.
- [6] Hasib Zunair, Aimon Rahman, and Nabeel Mohammed, "Estimating severity from ct scans of tuberculosis patients using 3d convolutional nets and slice selection," *CLEF (Working Notes)*, vol. 24, 2019.
- [7] Hasib Zunair, Aimon Rahman, Nabeel Mohammed, and Joseph Paul Cohen, "Uniformizing techniques to process ct scans with 3d cnns for tuberculosis prediction," in *Predictive Intelligence in Medicine: Third International Workshop, PRIME 2020, Held in Conjunction with MICCAI 2020, Lima, Peru, October 8, 2020, Proceedings 3*. Springer, 2020, pp. 156–168.
- [8] Ozan Sener and Silvio Savarese, "Active learning for convolutional neural networks: A core-set approach," in *International Conference on Learning Representations*, 2018.
- [9] Xiaoyang Wu, Yuyang Huo, Haojie Ren, and Changliang Zou, "Optimal subsampling via predictive inference," *Journal of the American Statistical Association*, vol. 119, no. 548, pp. 2844–2856, 2024.
- [10] Mei Zhang, Yongdao Zhou, Zheng Zhou, and Aijun Zhang, "Model-free subsampling method based on uniform designs," *IEEE Transactions on Knowledge and Data Engineering*, 2023.
- [11] Yichen Xie, Han Lu, Junchi Yan, Xiaokang Yang, Masayoshi Tomizuka, and Wei Zhan, "Active finetuning: Exploiting annotation budget in the pretraining-finetuning paradigm," in *Proceedings of the IEEE/CVF Conference on Computer Vision and Pattern Recognition*, 2023, pp. 23715–23724.
- [12] Xudong Wang, Long Lian, and Stella X Yu, "Unsupervised selective labeling for more effective semi-supervised learning," in *European Conference on Computer Vision*. Springer, 2022, pp. 427–445.
- [13] Lebede Ngartera, Mahamat Ali Issaka, and Saralees Nadarajah, "Application of bayesian neural networks in healthcare: Three case studies," *Machine Learning and Knowledge Extraction*, vol. 6, no. 4, pp. 2639–2658, 2024.
- [14] Balaji Lakshminarayanan, Alexander Pritzel, and Charles Blundell, "Simple and scalable predictive uncertainty estimation using deep ensembles," *Advances in neural information processing systems*, vol. 30, 2017.
- [15] Zeinab Abboud, Herve Lombaert, and Samuel Kadoury, "Sparse bayesian networks: Efficient uncertainty quantification in medical image analysis," in *International Conference on Medical Image Computing and Computer-Assisted Intervention*. Springer, 2024, pp. 675–684.
- [16] Yu A Malkov, "Efficient and robust approximate nearest neighbor search using hierarchical navigable small world graphs," *IEEE transactions on pattern analysis and machine intelligence*, vol. 42, no. 4, pp. 824–836, 2018.
- [17] Kuniaki Saito, Kohei Watanabe, Yoshitaka Ushiku, and Tatsuya Harada, "Maximum classifier discrepancy for unsupervised domain adaptation," in *Proceedings of the IEEE conference on computer vision and pattern recognition*, 2018, pp. 3723–3732.
- [18] Jae Won Cho, Dong-Jin Kim, Yunjae Jung, and In So Kweon, "Mcdal: Maximum classifier discrepancy for active learning," *IEEE transactions on neural networks and learning systems*, vol. 34, no. 11, pp. 8753–8763, 2022.
- [19] Nicola Fink, Jonathan I Sperl, Johannes Rueckel, Theresa Stüber, Sophia S Goller, Jan Rudolph, Felix Escher, Theresia Aschauer, Boj F Hoppe, Jens Ricke, et al., "Artificial intelligence-based automated matching of pulmonary nodules on follow-up chest ct," *European Radiology Experimental*, vol. 9, no. 1, pp. 48, 2025.
- [20] Julien Guiot, Monique Henket, Fanny Gester, Béatrice André, Benoit Ernst, Anne-Noelle Frix, Dirk Smeets, Simon Van Eyndhoven, Katerina Antoniou, Lennart Conemans, et al., "Automated ai-based image analysis for quantification and prediction of interstitial lung disease in systemic sclerosis patients," *Respiratory Research*, vol. 26, no. 1, pp. 39, 2025.
- [21] Zirui Zhu, "Advancements in automated classification of chronic obstructive pulmonary disease based on computed tomography imaging features through deep learning approaches," *Respiratory Medicine*, p. 107809, 2024.
- [22] Wu Quanyang, Huang Yao, Wang Sicong, Qi Linlin, Zhang Zewei, Hou Donghui, Li Hongjia, and Zhao Shijun, "Artificial intelligence in lung cancer screening: Detection, classification, prediction, and prognosis," *Cancer Medicine*, vol. 13, no. 7, pp. e7140, 2024.
- [23] Shirin Kordnoori, Maliheh Sabeti, Hamidreza Mostafaei, and Saeed Seyed Agha Banihashemi, "Lungxpertai: A deep multi-task learning model for chest ct scan analysis and covid-19 detection," *Biomedical Signal Processing and Control*, vol. 99, pp. 106866, 2025.
- [24] Joseph Needham, *Science and Civilisation in China: Volume 3, Mathematics and the Sciences of the Heavens and the Earth*, vol. 3, Cambridge University Press, 1959.
- [25] Carl De Boor, "Bicubic spline interpolation," *Journal of mathematics and physics*, vol. 41, no. 1–4, pp. 212–218, 1962.
- [26] Siegfried Graf and Harald Luschgy, *Foundations of quantization for probability distributions*, Springer, 2007.
- [27] Simon Mak and V Roshan Joseph, "Support points," *The Annals of Statistics*, vol. 46, no. 6A, pp. 2562–2592, 2018.
- [28] Yutian Chen, Max Welling, and Alex Smola, "Super-samples from kernel herding," *arXiv preprint arXiv:1203.3472*, 2012.
- [29] Eyke Hüllermeier and Willem Waegeman, "Aleatoric and epistemic uncertainty in machine learning: An introduction to concepts and methods," *Machine learning*, vol. 110, no. 3, pp. 457–506, 2021.
- [30] Tianyang Wang, Yunze Wang, Jun Zhou, Benji Peng, Xinyuan Song, Charles Zhang, Xintian Sun, Qian Niu, Junyu Liu, Silin Chen, et al., "From aleatoric to epistemic: Exploring uncertainty quantification techniques in artificial intelligence," *arXiv preprint arXiv:2501.03282*, 2025.
- [31] Radford M Neal, *Bayesian learning for neural networks*, vol. 118, Springer Science & Business Media, 2012.
- [32] Yarin Gal and Zoubin Ghahramani, "Dropout as a bayesian approximation: Representing model uncertainty in deep learning," in *international conference on machine learning*. PMLR, 2016, pp. 1050–1059.
- [33] Moloud Abdar, Farhad Pourpanah, Sadiq Hussain, Dana Rezazadegan, Li Liu, Mohammad Ghavamzadeh, Paul Fieguth, Xiaochun Cao, Abbas Khosravi, U Rajendra Acharya, et al., "A review of uncertainty quantification in deep learning: Techniques, applications and challenges," *Information fusion*, vol. 76, pp. 243–297, 2021.
- [34] Murat Sensoy, Lance Kaplan, and Melih Kandemir, "Evidential deep learning to quantify classification uncertainty," *Advances in neural information processing systems*, vol. 31, 2018.
- [35] Vladimir Vovk, Alexander Gammerman, and Glenn Shafer, *Algorithmic learning in a random world*, vol. 29, Springer, 2005.
- [36] Zifeng Wang, Zhenbang Wu, Dinesh Agarwal, and Jimeng Sun, "Med-clip: Contrastive learning from unpaired medical images and text," in *Proceedings of the 2022 Conference on Empirical Methods in Natural Language Processing*, 2022, pp. 3876–3887.
- [37] Samuli Laine and Timo Aila, "Temporal ensembling for semi-supervised learning," in *International Conference on Learning Representations*, 2016.
- [38] Shai Ben-David, John Blitzer, Koby Crammer, Alex Kulesza, Fernando Pereira, and Jennifer Wortman Vaughan, "A theory of learning from different domains," *Machine learning*, vol. 79, pp. 151–175, 2010.
- [39] Kang Zhang, Xiaohong Liu, Jun Shen, Zhihuan Li, Ye Sang, Xingwang Wu, Yunfei Zha, Wenhua Liang, Chengdi Wang, Ke Wang, et al., "Clinically applicable ai system for accurate diagnosis, quantitative

measurements, and prognosis of covid-19 pneumonia using computed tomography,” *Cell*, vol. 181, no. 6, pp. 1423–1433, 2020.

- [40] P Li, S Wang, T Li, J Lu, Y HuangFu, and D Wang, “A large-scale ct and pet/ct dataset for lung cancer diagnosis (lung-pet-ct-dx),” *Cancer Imaging Arch.*, 2020.
- [41] Kaiming He, Xiangyu Zhang, Shaoqing Ren, and Jian Sun, “Deep residual learning for image recognition,” in *Proceedings of the IEEE conference on computer vision and pattern recognition*, 2016, pp. 770–778.
- [42] Ashish Vaswani, Noam Shazeer, Niki Parmar, Jakob Uszkoreit, Llion Jones, Aidan N Gomez, Łukasz Kaiser, and Illia Polosukhin, “Attention is all you need,” *Advances in neural information processing systems*, vol. 30, 2017.
- [43] Haoqi Fan, Tullie Murrell, Heng Wang, Kalyan Vasudev Alwala, Yanghao Li, Yilei Li, Bo Xiong, Nikhila Ravi, Meng Li, Haichuan Yang, Jitendra Malik, Ross Girshick, Matt Feiszli, Aaron Adcock, Wan-Yen Lo, and Christoph Feichtenhofer, “PyTorchVideo: A deep learning library for video understanding,” in *Proceedings of the 29th ACM International Conference on Multimedia*, 2021, <https://pytorchvideo.org/>.
- [44] Kingma DP Ba J Adam et al., “A method for stochastic optimization,” *arXiv preprint arXiv:1412.6980*, vol. 1412, no. 6, 2014.

APPENDIX

A. Model Architecture of Coarse Screening

First, we employ a ResNet-34 [41] as the backbone for extracting features from each selected slice. We modify the standard ResNet-34 by replacing the final 1000-dimensional fully-connected (FC) layer with a 512-dimensional FC layer and removing the final softmax function. Then, the output of ResNet-34 is used as input to a light transformer-based network [42] for feature fusion, where both the layer number and the head number of the Transformer Encoder are set to 6. Finally, we perform an FC layer and a softmax function on the output of the network to predict the probability of disease.

To ensure fair comparison, we configure the same classification model for all sub-sampling methods and compare the performance of models trained with data sub-sampled by different methods. Although the feature extraction process is at the slice level, we fuse them, and the model prediction output is at the patient level, so there is no data leakage problem, that is, slices from the same patient could not appear in both the training set and the validation set. In addition, it is worth noting that the full CT method uses 3D-ResNet [43] as the classification model, therefore, there will be no data leakage problem.

B. Implementations Details

1) *Computer Resources*: All models are implemented in PyTorch and trained on an RTX 4090 with 24 GB memory.

2) *Sub-Sampling*: **CSS**: The CSS process is described in the main text, so we will not reiterate it here. Below, we provide the specific hyperparameter settings as follows: $k = 10$, $\alpha = 0.5$, $\beta = 0.9$, $\lambda = 0.5$, and $T = 10$. It is worth noting that in the CSS method, the distance between each instance and its k -th nearest neighbor can be sensitive to noise, as it relies solely on the k -th nearest neighbor. Following the settings of [12], we modify this by using the average distance to the k nearest neighbors, denoted as $\bar{D}(z_i^j, k) = \frac{1}{k} \sum_{l=1}^k D(z_i^j, z_i^j|l)$.

CoreSet [8] and ActiveFT [11]: For fair comparison, we set the preprocessing steps (*i.e.*, feature extraction) and the lung

patching process of the CoreSet and ActiveFT to be consistent with the CSS, and then perform slice selection according to their respective strategies. Their respective strategies can be found in the original paper, and are not described here again.

PI, LI and SI: Interpolation methods calculate the new pixel value in the compressed image based on the values of surrounding pixels on the Z -axis.

SSS: SSS selects $m/3$ slices from the first, middle, and last positions of the CT volume, respectively.

ESS: ESS selects one after every $\lfloor n/m \rfloor$ of slices.

3) *Classification Model Training*: During the classification model training, we use Adam [44] with an initial learning rate $1e^{-3}$ to optimize the network. We set different batch sizes for experiments with different numbers of selected slices. The more slices selected for each case, the more GPU memory each case occupies; thus, the batch size should be smaller. In detail, batch size = 1, 4, 8, 16, 16 is set for $m = 64, 32, 16, 8, 4$ respectively. For a fair comparison, the training epoch of all experiments is set to 400.

4) *Uncertainty Quantification*: To ensure a fair comparison of the performance of UQ methods, the classification prediction outcomes of the models must remain consistent. Some UQ methods produce multiple outputs, such as the DE methods, which integrate predictions from multiple models, and the discrepancy-only methods, which employ multiple classifiers. To address this, we establish a primary model (*i.e.*, ResNet-34) for all methods, ensuring identical initialization and training configurations. Specifically, this model is trained using CT data sub-sampled via CSS, with the number of sub-sampled slices set to 32. This approach guarantees consistent classification predictions across all methods while allowing different approaches to incorporate outputs from auxiliary branches during the UQ phase.

Entropy-only method: The entropy of the predicted probability vector is used as the uncertainty measure. For sample \tilde{x}_i , entropy is calculated as: $\mathcal{H}(\tilde{x}_i) = -\sum_{j=1}^K p_{i,j} \log p_{i,j}$, where $p_{i,j}$ denotes the j -th element of \mathbf{p}_i .

Discrepancy-only method: This method employs the same model structure and training protocol as AUQ, but utilizes only discrepancy as the uncertainty metric. The discrepancy calculation is denoted as Equation (4) in the main text.

DE method: Two auxiliary deep models are trained. Their architectures and training settings match the primary model, but with different initializations. During the UQ phase, the predictive probabilities of all three models are averaged, after which entropy is computed as the uncertainty measure.

MC Dropout method: An additional neural network with Dropout layers is trained. It shares the same architecture as the primary model but includes Dropout layers (rate = 0.5) after each block. During the UQ phase, this model performs two additional forward passes. Its outputs are averaged with those of the primary model, and entropy is subsequently computed as the uncertainty measure.

TABLE VI
COMPARISON UNDER EXTREME SUB-SAMPLING.

Number	Method	Task 1		Task 2		Task 3	
		Accuracy	Recall	Accuracy	Recall	Accuracy	Recall
16	SI	96.99 ± 1.55	97.21 ± 1.10	93.87 ± 2.27	94.07 ± 2.03	76.71 ± 2.70	76.90 ± 2.56
	ActiveFT	96.94 ± 0.87	97.19 ± 0.88	93.61 ± 1.48	94.20 ± 1.95	78.95 ± 2.11	79.43 ± 2.03
	CSS (Ours)	97.26 ± 1.54	97.58 ± 1.21	94.00 ± 2.15	94.28 ± 2.04	85.60 ± 2.37	85.54 ± 2.40
8	SI	95.96 ± 1.19	95.88 ± 1.22	92.09 ± 2.77	92.55 ± 2.49	67.34 ± 3.83	67.68 ± 3.41
	ActiveFT	96.13 ± 1.11	96.12 ± 1.43	92.42 ± 1.75	92.98 ± 2.28	74.61 ± 3.13	75.24 ± 2.41
	CSS (Ours)	96.57 ± 1.24	96.89 ± 1.27	93.21 ± 3.72	93.02 ± 3.44	82.55 ± 2.32	82.63 ± 2.17
4	SI	93.86 ± 2.24	94.24 ± 1.89	90.03 ± 2.25	90.78 ± 2.30	64.41 ± 3.70	64.57 ± 3.54
	ActiveFT	94.07 ± 1.40	94.51 ± 2.02	90.79 ± 2.08	91.23 ± 2.44	70.72 ± 3.41	69.14 ± 2.98
	CSS (Ours)	94.90 ± 2.12	95.19 ± 2.01	91.17 ± 2.54	91.76 ± 2.51	78.64 ± 3.19	78.89 ± 2.98

C. Additional Comparison with Other Sub-Sampling Methods

We compare CSS with SI and ActiveFT under extreme sub-sampling, that is, selecting 16, 8, and 4 CT slices from each case. The experimental results are shown in Table VI, from which we can observe that our method outperforms other methods, especially on the difficult task 3. For instance, at Number = 4, CSS achieved an accuracy of 78.64% and a recall of 78.89%. Although this shows a significant drop compared to results with higher sampling rates, it surpasses the second-best method ActiveFT by 7.92% in accuracy and 9.75% in recall. This demonstrates that under extreme sub-sampling scenarios, our method holds a greater advantage.